State Estimation of Hemodynamic Model for fMRI Under Confounds: SSM Method

Haifeng Wu, Mingzhi Lu, and Yu Zeng

***Abstract*—Through hemodynamic models, the change of neuronal state can be estimated from functional magnetic resonance imaging (fMRI) signals. Usually, there are confounds in the fMRI signal, which will degrade the performance of the estimation for the neuronal state change. For the reason, this paper introduces a state space model (SSM) with confounds, from a conventional hemodynamic model. In this model, a successive state estimation method requires a state value vector, an error covariance, an innovation covariance and a cross covariance to be re-derived. Thus, a confounds square-root cubature Kalman smoothing (CSCKS) algorithm is proposed in this paper. We use a Balloon-Windkessel model to generate simulation data and add confounds signals to evaluate the performance of the proposed algorithm. The experiment results show that when the signal-to-interference ratio (SIR) is less than 21 dB, the CSCKS proposed in this paper reduced estimation error to 16%, whereas the traditional algorithm reduced it to only 73%.**

***Index Terms*—fMRI, confounds, hemodynamic model.**

I. Introduction

BECAUSE functional magnetic resonance imaging (fMRI) technology has the advantage of non-invasive, non-radiative, repeatable and accurate positioning, and has high temporal and spatial resolution, it has become an important imaging technology applied to brain function and clinical research. In brain cognitive activity, neuronal changes are a dynamic process that produces a series of hemodynamic responses in the region of the neuronal population or source. The responses are manifested by changes in cerebral blood flow and blood oxygen concentration as neurons change. The fMRI technique measures the responses and uses hemodynamics to study the neuronal activation of the brain regions [1]-[2], so hemodynamic studies are critical for the application of fMRI to studies of brain function.

The relationship between neuronal state changes in functional brain regions and blood flow, blood oxygen concentration and other measured values is a complex electrophysiological process [3], which can be described by state space models. For instance, differential equations could be used to establish a hemodynamic model [2], where the neuronal activation is associated with a series of parameters, which mainly consists of two parts. The first is a coupling process that describes how neuronal activity induces blood changes. The second is a hemodynamic process that describes the changes of cerebral blood flow, cerebral blood volume, and total deoxyhemoglobin content. Through the inversion of the state space model, we can use brain blood observations to estimate changes in the hidden neuronal state and make inferences about neuronal coupling (see below).

The hemodynamic model described by the differential equations is not only dynamic but also highly nonlinear [6]-[7]. For this nonlinear problem, many researchers have proposed various algorithms to estimate the hidden neuron state or related parameters of the model [8]-[23], [26], [31], where Friston et al. conducted a more in-depth study of the problem. First, they used a Volterra series kernel to estimate the hemodynamic model parameters [8], and then proposed to use Bayesian estimation theory to invert the hemodynamic model [10]. Next, they extended the algorithm to coupled neuronal sources, where the connection parameters of distinct brain regions were estimated [11]. These brain-regions coupling models are called dynamic causal models (DCM). In recent years, DCM has been widely used in analysis of effective connectivity and electrophysiological studies in functional brain architectures. In order to consider the effects of physiological and stochastic noise [14]-[15], Riera et al. considered a stochastic model [16], which uses a local linearization filter (LLF) [18] and parameterized radial basis functions (RBFs) [16] to estimate hidden neuron states and model parameters. In addition, a successive state estimation method was shown to solve the nonlinear problem of hemodynamic model inversion. Johnston et al. [19] used a particle filter algorithm to estimate hidden neural states, and it was found its performance was better than LLF. Murray et al. [20] proposed a two-direction particle filter algorithm based on this method, and others have used the unscented Kalman filter (UKF) [22], which both show better performance in state estimation under nonlinear conditions.

However, sometimes we need to know both the hidden

This work is supported by the National Natural Science Foundation of China (61762093), the 17th Batch of Young and Middle-aged Leaders in Academic and Technical Reserved Talents Project of Yunnan Province (2014HB019), Program for Innovative Research Team (in Science and Technology) in University of Yunnan Province, the Key Applied and Basic Research Foundation of Yunnan Province (2018FA036), and the Graduate Innovation Fund of Yunnan Minzu University (2018YJCXS169). (Corresponding author: Haifeng Wu).

Haifeng Wu is with the School of Electrical and Information Technology, Yunnan Minzu University, Kunming, 650504, China. (correspondence e-mail: whf5469@gmail.com).

Mingzhi Lu is with the School of Electrical and Information Technology, Yunnan Minzu University, Kunming, 650504, China.(e-mail: mingzhilu@126.com).

Yu Zeng is with the School of Electrical and Information Technology, Yunnan Minzu University, Kunming, 650504, China. (e-mail: yv.zeng@gmail.com).

neuron states and model parameters. In brain cognitive activities, for example, we may care about which functional areas are activated and what is the effective connection among the activation regions [11]. At this time, most of the above methods cannot jointly estimate the hidden states and parameters unless a priori information of some model parameters is available. The dynamic expectation maximum (DEM) algorithm proposed by Friston [23] can effectively jointly estimate hidden states, input and parameters, and show robustness in the high nonlinear and dynamic systems [23]. The DEM algorithm is based on a state space model (SSM). A square-root cubature Kalman smoothing (SCKS) algorithm [3] proposed in recent years is also based on the SSM, which can jointly estimates the hidden states, input and parameters. Especially, when the integration step of the algorithm decreases, its estimation performance is better than the DEM algorithm. However, the fMRI signal usually has confounds, which are caused by peripheral factors such as physiological fluctuations, measuring instruments and the external environment [27]. Even filtering methods can only partially eliminate the confounds [28]-[30], [32]. The existing SCKS method does not consider the possible confounds and thus its estimation performance will be affected.

For this reason, this paper establishes a new SSM equation with confounds, based on the original differential equations of the hemodynamic model. Since the new SSM equation considers the confounds, the existing SCKS method is no longer applicable. Hence, we redefine the vectors of the hidden states and the observed states, and then derive the corresponding variance matrix and innovation matrix. Next, the hidden states and model parameters are estimated via a cubature Kalman filter. Experimental results show that the confounds square-root cubature Kalman smoothing (CSCKS) algorithm proposed in this paper is better than the existing algorithms in estimating the hidden states when the signal to interference (i.e., confounds) ratio (SIR) is relatively small.

II. Related Methods of Hemodynamic SSM for FMRI

In general, an fMRI hemodynamic model can be described by differential equations [2]-[3], [6]-[7], [23]. Without loss of generality, the differential equations are expressed as

$$\dot{\mathbf{x}} = \mathbf{f}\left(\mathbf{x}, u, \boldsymbol{\theta}\right), \tag{1-a}$$

$$y = g\left(\mathbf{x}, u, \boldsymbol{\theta}\right), \tag{1-b}$$

where

$\mathbf{x}$ is a hidden state vector, $\dot{\mathbf{x}}$ is a differential of $\mathbf{x}$,

u is an external input,

$\boldsymbol{\theta}$ is a biophysical parameter vector for the model,

y is a observed blood oxygen level dependent (BOLD) signal,

$\mathbf{f}(\cdot)$ and $g(\cdot)$ are a state function and a observation function of the model, respectively.

As can be seen from (1), the model expresses the changes of neuron state as a series of parameters of brain blood, and the change of the neuronal state can be estimated from the observation of BOLD signal by the inversion of the equation.

DEM algorithm is a method for the state estimation of the hemodynamic model. It constructs a group of equations using generalized coordinates of motion [23].

$$D\tilde{\mathbf{x}} = \tilde{\mathbf{f}}, \tag{2-a}$$

$$D\tilde{\mathbf{y}} = \tilde{\mathbf{g}}, \tag{2-b}$$

where

$\tilde{\mathbf{g}}$ denotes a column vector from the 0th, the 1th, ... order differentials for the function $g(\cdot)$,

$\tilde{\mathbf{y}}$ denotes a column vector from the 0th, 1th, ... order differentials for y,

$\tilde{\mathbf{f}}$ denotes a column vector from the 0th, 1th, ...order full differential for the function $\mathbf{f}(\cdot)$.

$\tilde{\mathbf{x}}$ denotes a column vector from the 0th, the 1th, ...order differential of $\mathbf{x}$,

D denotes a differential matrix operator.

Equation (2) is actually a group of SSM equations, and the DEM algorithm uses the principle of the dynamic expectation maximization (EM) algorithm to solve the hidden states $\mathbf{x}$ of neurons. Compared with the traditional inversion method, the advantage of the SSM-based DEM algorithm is that not only the hidden states $\mathbf{x}$ but also the corresponding model parameters $\boldsymbol{\theta}$ can be estimated. In some situations that require knowing both neuronal states and other model parameters, DEM has an advantage over algorithms that can only estimate neuronal states.

SCKS algorithm is also a SSM method based on the model in (2), which uses local linearization [3] to construct the equation of SSM, and then uses a cubature Kalman filter (CKF) to solve the state values. Since $\mathbf{x}$, u and $\boldsymbol{\theta}$ are parameters w.r.t. time t, we could let $\mathbf{x}_t$, u_t and $\boldsymbol{\theta}_t$ be the value of $\mathbf{x}$, u and $\boldsymbol{\theta}$ at time t, respectively. Further, let $t = n\Delta t$ where Δt is an integration step. Thus,

$$\mathbf{x}_{n\Delta t} = \mathbf{x}_{(n-1)\Delta t} + \int_{(n-1)\Delta t}^{n\Delta t} \mathbf{f}\left(\mathbf{x}_{(n-1)\Delta t}, u_{n\Delta t}, \boldsymbol{\theta}_{n\Delta t}, t\right) dt, \tag{3}$$

After local linearization of (3) and omitting Δt, we will give the following augmented SSM equation

$$\bar{\mathbf{x}}_n = \mathbf{H}\left(\bar{\mathbf{x}}_{n-1}\right) + \mathbf{P}_{n-1}, \tag{4-a}$$

$$y_n = g\left(\bar{\mathbf{x}}_n\right) + m_n, \tag{4-b}$$

where

$\bar{\mathbf{x}}_n = [\,\mathbf{x}_n, u_n, \boldsymbol{\theta}_n\,]^{\mathrm{T}}$,

$\mathbf{H}\left(\bar{\mathbf{x}}_{n-1}\right) = [\,\mathbf{h}\left(\bar{\mathbf{x}}_{n-1}, u_n, \boldsymbol{\theta}_n\right), \boldsymbol{\theta}_{n-1}\,]^{\mathrm{T}}$,

$\mathbf{h}\left(\mathbf{x}_{n-1}, u_n, \boldsymbol{\theta}_n\right) \approx \mathbf{x}_{n-1} + \mathbf{J}^{-1}\left[\exp\left(\mathbf{J}\Delta t\right) - \mathrm{I}\right]\mathbf{f}\left(\mathbf{x}_{n-1}, u_n, \boldsymbol{\theta}_n, t\right)$,

$\mathbf{J}$ denotes the Jacobian determinant of $\mathbf{f}(\cdot)$ w.r.t. $\mathbf{x}_n$,

$\mathbf{P}_{n-1} = [\,\mathbf{p}_{n-1}, \mathbf{s}_{n-1}\,]^{\mathrm{T}}$ is a zero-mean Gaussian white noise vector whose autocovariance matrix is a diagonal matrix,

$\mathbf{p}_{n-1}$, $\mathbf{s}_{n-1}$ and m_n are zero-mean Gaussian white noise vectors corresponding to $\mathbf{x}_n$, $\boldsymbol{\theta}_n$ and y_n, respectively whose autocovariance matrices are also diagonal.

It can be seen from (4) that like DEM algorithm, the SSM used by the SCKS scheme can jointly estimate the hidden states $\mathbf{x}_n$ and biophysical parameters $\boldsymbol{\theta}_n$. In particular, when the integral step Δt decreases, the estimation error of SCKS will be smaller than DEM algorithm [3].

In summary, we have reviewed the distinction between the state space models used for estimation of hidden states $\mathbf{x}$ (i.e., Equation 1) and augmented models that allow for estimation of both hidden states $\mathbf{x}_n$ and biophysical parameters $\boldsymbol{\theta}_n$ (i.e.,

This article has been accepted for publication in a future issue of this journal, but has not been fully edited. Content may change prior to final publication. Citation information: DOI 10.1109/JBHI.2019.2917093, IEEE Journal of Biomedical and Health Informatics

Equation 4). This rests upon augmenting hidden states $\mathbf{x}_n$ with a parameter vector $\boldsymbol{\theta}_n$ – so that both are estimated during filtering. Crucially, the noise variance on the estimated parameters $\mathbf{x}_n$ and $\boldsymbol{\theta}_n$ is assumed to be very small, so that it is effectively estimated as a constant over the time series. This device (i.e., augmentation of a state space with parameters) could, in principle, be applied in the context of any filtering scheme. And then, cubature filtering can be applied to this augmentation with implementations of estimation.

III. Problem Of Confounds In SSM

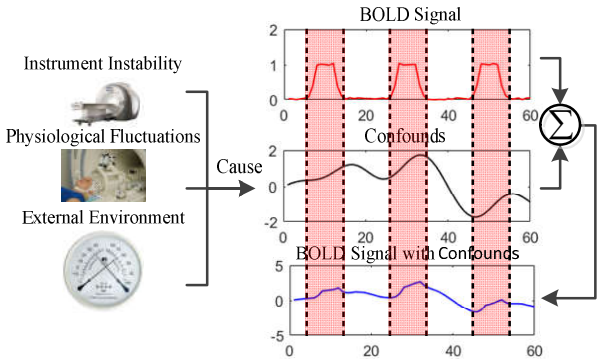

Fig. 1. Schematic for confounds.

The confounds of fMRI signals are mainly caused by scanner instability and some physiological factors, such as the heartbeat and respiration of subjects [27]. At present, the repetition time (TR) of fMRI using EPI technology is about 2-3 seconds [28], while the average person's hearting and breathing frequency are about 1 Hz and 0.3 Hz [28], respectively which are close to the scanner sampling frequency. Filters such as low pass, high pass and notch can only filter out some of the confounds [29]-[32]. Therefore, confounds in fMRI signals are a common phenomenon. When the fMRI signal is superimposed with the confounds, low-frequency drifts occurs, as shown in Fig. 1. In this case, the original SSM equation in (4) becomes

$$\bar{\mathbf{x}}_n = \mathbf{H}\left(\bar{\mathbf{x}}_{n-1}\right) + \mathbf{P}_{n-1}, \tag{5-a}$$

$$y_n = g\left(\bar{\mathbf{x}}_n\right) + C_n + m_n, \tag{5-b}$$

where C_n is the signal obtained by superimposing the confounds. Since the existing SCKS method does not consider the confounds, C_n can only be regarded as noise and merged into m_n when solving the state $\bar{\mathbf{x}}_n$ in (5). SCKS uses a CKF filter to complete the estimation of hidden states and biophysical parameters. Only when the noise of the observation equation obeys a Gaussian white noise, however, Bayesian optimality conditions are satisfied. Unfortunately, the combined noise does not necessarily satisfy the condition. Therefore, once the fMRI signal contains more confounds, the estimation performance of SCKS will inevitably be affected.

IV. SSM Under Confounds

In order to reduce the influence of confounds on estimation of state, we need to rewrite the original state equation. The confounds C_n can be approximately expressed as trigonometric series expansion [11], i.e.

$$C_n = \boldsymbol{\beta}_n^{\mathrm{T}} \boldsymbol{\Omega}_n, \tag{6}$$

where

$\boldsymbol{\Omega}_n = [\sqrt{1/L}\cos 0\omega n\Delta t, \sqrt{2/L}\cos 1\omega n\Delta t, \ldots \sqrt{2/L}\cos\left(\bar{L}-1\right)\omega n\Delta t]^{\mathrm{T}}$, $n = 1,2,\ldots L$,

ω denotes a nominal angular frequency,

$\boldsymbol{\beta}_n = a\boldsymbol{\beta}'_n$ denotes the coefficient vector of the confounds, i.e. the coefficient of the Fourier series,

a denotes the amplitude of confounds,

$\boldsymbol{\beta}'_n = [b_{0,n}, b_{1,n}, \ldots b_{(\bar{L}-1),n}]^{\mathrm{T}}$,

$\bar{L}$ denotes the maximum order of the harmonics of the trigonometric function.

Note that the confounds in (6) are approximately expressed as some trigonometric series with a fixed angular frequency. In practice, cardiac and respiration signals in confounds are not stationary and also not independent of each other. The rate of the cardiac signal and respiration interact with each other, and even with input stimuli. In simulation, we model confounds as trigonometric series with time-variable frequencies, where each component are correlated. The details can be seen in Section VI. Then, we use the approximate expression of (6) to estimate the simulated confounds.

Substituting (6) into (5) and rewriting the SSM will have the following augmented SSM equation

$$\mathbf{x}'_n = \mathbf{H}'\left(\mathbf{x}'_{n-1}\right) + \mathbf{P}'_{n-1}, \tag{7-a}$$

$$y_n = \lambda\left(\mathbf{x}'_n\right) + m_n, \tag{7-b}$$

where

$\mathbf{x}'_n = [\mathbf{x}_n, \boldsymbol{\theta}_n, \boldsymbol{\beta}_n]^{\mathrm{T}}$,

$\mathbf{H}'\left(\mathbf{x}'_{n-1}\right) = [\mathbf{h}\left(\mathbf{x}_{n-1}, u_n, \boldsymbol{\theta}_n\right), \boldsymbol{\theta}_{n-1}, \boldsymbol{\beta}_{n-1}]^{\mathrm{T}}$,

$\mathbf{P}'_{n-1} = [\mathbf{p}_{n-1}, \mathbf{s}_{n-1}, \mathbf{v}_{n-1}]^{\mathrm{T}}$ is also a zero-mean Gaussian white noise vector, and its autocovariance matrix is also a diagonal matrix.

$\lambda\left(\mathbf{x}'_n\right) = g\left(\mathbf{x}_n, u_n, \boldsymbol{\theta}_n\right) + \boldsymbol{\beta}_n^{\mathrm{T}}\boldsymbol{\Omega}_n$.

It can be seen from (7) that the augmented variable $\mathbf{x}'_n$ now includes parameters $\boldsymbol{\beta}_n$ controlling confounding fluctuations in the observed signal, compared with the state vector $\bar{\mathbf{x}}_n$ in the SSM in (4). Like (4), in other word, (7) uses exactly the same augmentation device, we have now absorbed these confounds parameters into the augmented state vector $\mathbf{x}'_n$ – and have equipped them with a low variance. In this model, the confounds are no longer regarded as noise, but are expanded by the Fourier series, and the coefficients $\boldsymbol{\beta}_n$ of the series are directly estimated.

In the section of model, we will take this augmentation one step further and absorb parameters controlling fluctuations such as confounds in fMRI time series in (7). This provides a complete model of how hemodynamic states are generated under unknown parameters controlling both the neuronal dynamics and non-neuronal compounds. Note that by absorbing the parameters $\boldsymbol{\beta}_n$ into the augmented state vector $\mathbf{x}'_n$ in (7), we can now use standard filtering schemes under local linear assumptions in (3) and thereby access efficient estimates about hidden states $\mathbf{x}_n$, biophysical parameters $\boldsymbol{\theta}_n$ and the coefficients $\boldsymbol{\beta}_n$ of the confounds. The slight price paid for this is that the linearization implicit in (7) renders the filtering approximate for highly nonlinear systems.

It is worth noting that the purpose of the hemodynamic model studied in this paper is to estimate the hidden states and

biological parameters of the model through the observed BOLD signal, so as to clarify the state of the neurons in the brain region and the relationship among them. The existing SCKS not only estimates the hidden state $\mathbf{x}_n$ and parameter $\boldsymbol{\theta}_n$, but also estimates the input stimulus u_n. The external input is an external stimulus that induces changes in the hidden states and biological parameters of the model. In some fMRI experiments for brain cognitive, these external stimuli can be pre-designed and have a corresponding relationship with the external input u_n. For this reason, u_n can be used as a known variable and need not be estimated. Thus, the establish of (7) focus more on the hidden state $\mathbf{x}_n$ and parameter $\boldsymbol{\theta}_n$, and introduce another coefficient $\boldsymbol{\beta}_n$. That is, the model of (7) let $\boldsymbol{\beta}_n$ replaces u_n.

V. CSCKS ALGORITHM

For the SSM equation in (7), due to the confounds, the predicted estimation vector of state, predicted error covariance matrix, innovation covariance matrix and cross-covariance matrix involved in the existing SCKS algorithm need to be re-derived. Hence, the CSCKS algorithm is proposed for the state estimation in the SSM equation with confounds. The algorithm also uses a CKF filter to estimate model parameters, which can be divided into three steps, filter initialization, forward filtering and backward smoothing. Forward filtering can be further divided into a time update step and a measurement update step. Below, we will describe them, respectively.

A. Filter Initialization

Firstly, the initial augmented state vector $\hat{\mathbf{x}}^a_{0|0}$ needs to be assigned to

$$\hat{\mathbf{x}}^a_{0|0} = \left[\hat{\mathbf{x}}'_{0|0}, \mathbf{0}_{n_\mathbf{p}}, \mathbf{0}_{n_\mathbf{s}} \mathbf{0}_{n_\mathbf{v}}, \mathbf{0}_{n_m}\right]^{\mathrm{T}}, \tag{8}$$

where

$\hat{\mathbf{x}}'_{0|0} = [\hat{\mathbf{x}}_{0|0}, \hat{\boldsymbol{\theta}}_{0|0}, \hat{\boldsymbol{\beta}}_{0|0}]$,

$\hat{\mathbf{x}}_{0|0}$, $\hat{\boldsymbol{\theta}}_{0|0}$ and $\boldsymbol{\beta}_{0|0}$ denote the estimated values of the hidden states $\mathbf{x}$, biophysical parameters $\boldsymbol{\theta}$, and coefficients $\boldsymbol{\beta}$ of confounds at time 0, respectively

$\mathbf{0}_{n_\mathbf{p}}$, $\mathbf{0}_{n_\mathbf{s}}$, $\mathbf{0}_{n_\mathbf{v}}$ and $\mathbf{0}_{n_m}$ are all zero vectors and denote the values of corresponding dynamic noises $\mathbf{p}$, $\mathbf{s}$, $\mathbf{v}$ and m of $\mathbf{x}$, $\boldsymbol{\theta}$, $\boldsymbol{\beta}$ and y at time 0,

$n_\mathbf{p}$, $n_\mathbf{s}$, $n_\mathbf{v}$ and n_m denote the corresponding dimensions of the vectors $\mathbf{p}$, $\mathbf{s}$, $\mathbf{v}$ and m.

Next, the initial square root $\mathbf{S}^a_{0|0}$ of the corresponding error-covariance matrix is assigned to

$$\begin{aligned}\mathbf{S}^a_{0|0} &= chol\left(E\left[\left(\mathbf{x}^a_{0|0} - \hat{\mathbf{x}}^a_{0|0}\right)\left(\mathbf{x}^a_{0|0} - \hat{\mathbf{x}}^a_{0|0}\right)^{\mathrm{T}}\right]\right) \\ &= diag\left(\mathbf{S}_{0|0}, \mathbf{S}_\mathbf{p}, \mathbf{S}_\mathbf{s}, \mathbf{S}_\mathbf{v}, \mathrm{S}_m\right),\end{aligned} \tag{9}$$

where

$\mathbf{S}_{0|0} = diag(\mathbf{S}_{\mathbf{x},0|0}, \mathbf{S}_{\boldsymbol{\theta},0|0}, \mathbf{S}_{\boldsymbol{\beta},0|0})$,

$\mathbf{S}_{\mathbf{x},0|0} = \sqrt{\mathbf{Q}_{\mathbf{x},0|0}}$, $\mathbf{S}_{\boldsymbol{\theta},0|0} = \sqrt{\mathbf{Q}_{\boldsymbol{\theta},0|0}}$, $\mathbf{S}_{\boldsymbol{\beta},0|0} = \sqrt{\mathbf{Q}_{\boldsymbol{\beta},0|0}}$,

$\mathbf{S}_\mathbf{p} = \sqrt{\mathbf{Q}_\mathbf{p}}$, $\mathbf{S}_\mathbf{s} = \sqrt{\mathbf{Q}_\mathbf{s}}$, $\mathbf{S}_\mathbf{v} = \sqrt{\mathbf{Q}_\mathbf{v}}$, $S_m = \sqrt{Q_m}$.

$\mathbf{Q}_{\mathbf{x},0|0}$, $\mathbf{Q}_{\boldsymbol{\theta},0|0}$ and $\mathbf{Q}_{\boldsymbol{\beta},0|0}$ denote the error-covariance matrices of $\mathbf{x}$, $\boldsymbol{\theta}$ and $\boldsymbol{\beta}$ at time 0, respectively

$\mathbf{Q}_\mathbf{p}$, $\mathbf{Q}_\mathbf{s}$, $\mathbf{Q}_\mathbf{v}$ and Q_m denote the covariance matrix of the dynamic noise $\mathbf{p}$, $\mathbf{s}$, $\mathbf{v}$ and measurement noise m at time 0, respectively

chol denotes the Cholesky decomposition operation,

diag denotes a diagonal matrix.

B. Forward Filtering

The first step of the forward filtering is time update. Calculating numerical integral points will have

$$\boldsymbol{\chi}^a_{i,n-1|n-1} = \mathbf{S}^a_{n-1|n-1}\boldsymbol{\xi}_i + \hat{\mathbf{x}}^a_{n-1|n-1}, \tag{10}$$

where

$\boldsymbol{\xi}_i$ denotes a vector made up of the elements of the i th column of the integral points matrix $\boldsymbol{\Xi}$,

$\boldsymbol{\Xi} = \sqrt{\bar{m}/2}\ [\mathbf{I}, -\mathbf{I}]$,

$\mathbf{I} \in \mathbb{R}^{N\times N}$ denotes a unit matrix,

$\bar{m} = 2N$ is the number of numerical integral points,

$N = n_\mathbf{x} + n_{\boldsymbol{\theta}} + n_{\boldsymbol{\beta}} + n_\mathbf{p} + n_\mathbf{s} + n_\mathbf{v} + n_m$,

$n_\mathbf{x}$, $n_{\boldsymbol{\theta}}$ and $n_{\boldsymbol{\beta}}$ denotes the corresponding dimension of $\mathbf{x}$, $\boldsymbol{\theta}$ and $\boldsymbol{\beta}$ respectively,

$n = 1, 2, \ldots L$,

L denotes the length of y.

Substituting (10) into (7-a) and adding dynamic noise will have

$$\boldsymbol{\chi}^{\mathbf{x},\boldsymbol{\theta},\boldsymbol{\beta}}_{i,n|n-1} = \mathbf{H}'\left(\boldsymbol{\chi}^\mathbf{x}_{i,n-1|n-1}, \boldsymbol{\chi}^{\boldsymbol{\theta}}_{i,n-1|n-1}, \boldsymbol{\chi}^{\boldsymbol{\beta}}_{i,n-1|n-1}\right) + \boldsymbol{\chi}^{\mathbf{p},\mathbf{s},\mathbf{v}}_{i,n|n-1}, \tag{11}$$

where the superscript is used to distinguish the components of the numerical integral points. For example $\boldsymbol{\chi}^\mathbf{x}_{i,n-1|n-1}$, $\boldsymbol{\chi}^{\boldsymbol{\theta}}_{i,n-1|n-1}$ and $\boldsymbol{\chi}^{\boldsymbol{\beta}}_{i,n-1|n-1}$ denotes the corresponding numerical integral points of the components $\hat{\mathbf{x}}_{n-1|n-1}$, $\hat{\boldsymbol{\theta}}_{n-1|n-1}$ and $\hat{\boldsymbol{\beta}}_{n-1|n-1}$ in $\boldsymbol{\chi}^{\mathbf{x},\boldsymbol{\theta},\boldsymbol{\beta}}_{i,n-1|n-1} \in \mathbb{R}^{(n_\mathbf{x}+n_{\boldsymbol{\theta}}+n_{\boldsymbol{\beta}})\times 1}$, respectively. Then, calculate the predicted estimation $\hat{\mathbf{x}}'_{n|n-1}$ of the states and the square root $\mathbf{S}_{n|n-1}$ of the predicted error-covariance of the states

$$\hat{\mathbf{x}}'_{n|n-1} = \left(\sum_{i=1}^{\bar{m}} \boldsymbol{\chi}^{\mathbf{x},\boldsymbol{\theta},\boldsymbol{\beta}}_{i,n|n-1}\right) \Big/ \bar{m}, \tag{12}$$

$$\mathbf{S}_{n|n-1} = qr\left(\left[\mathbf{X}_{n|n-1}\right]\right), \tag{13}$$

where

$$\mathbf{X}_{n|n-1} = \left[\boldsymbol{\chi}^{\mathbf{x},\boldsymbol{\theta},\boldsymbol{\beta}}_{1,n|n-1} - \hat{\mathbf{x}}'_{n|n-1}, \boldsymbol{\chi}^{\mathbf{x},\boldsymbol{\theta},\boldsymbol{\beta}}_{2,n|n-1} - \hat{\mathbf{x}}'_{n|n-1}, \ldots, \boldsymbol{\chi}^{\mathbf{x},\boldsymbol{\theta},\boldsymbol{\beta}}_{\bar{m},n|n-1} - \hat{\mathbf{x}}'_{n|n-1}\right] \Big/ \sqrt{\bar{m}}, \tag{14}$$

and *qr* denotes QR decomposition.

The second step is measurement update. Substituting (10) into (7-b) and adding the measurement noise will have

$$\Psi_{i,n|n-1} = \lambda\left(\boldsymbol{\chi}^\mathbf{x}_{i,n|n-1}, \boldsymbol{\chi}^{\boldsymbol{\theta}}_{i,n|n-1}, \boldsymbol{\chi}^{\boldsymbol{\beta}}_{i,n|n-1}\right) + \boldsymbol{\chi}^m_{i,n-1|n-1}, \tag{15}$$

Then, the predicted estimation of the measured BOLD signal is

$$\hat{y}_{n|n-1} = \sum_{i=1}^{\bar{m}} \Psi_{i,n|n-1}, \tag{16}$$

Hence, we could calculate the innovation covariance $\mathbf{S}_{yy,n|n-1}$ and the cross-covariance matrix $\bar{\mathbf{P}}_{xy,n|n-1}$

$$\mathbf{S}_{yy,n|n-1} = qr\left(\left[\mathbf{Y}_{n|n-1}\right]\right), \tag{17}$$

$$\bar{\mathbf{P}}_{xy,n|n-1} = \mathbf{X}_{n|n-1}\mathbf{Y}^{\mathrm{T}}_{n|n-1}, \tag{18}$$

where

$$\mathbf{Y}_{n|n-1} = \left[\Psi_{1,n|n-1} - \hat{\mathrm{y}}_{n|n-1}, \Psi_{2,n|n-1} - \hat{\mathrm{y}}_{n|n-1}, \ldots, \Psi_{\bar{m},n|n-1} - \hat{\mathrm{y}}_{n|n-1}\right] \Big/ \sqrt{\bar{m}},$$

This article has been accepted for publication in a future issue of this journal, but has not been fully edited. Content may change prior to final publication. Citation information: DOI 10.1109/JBHI.2019.2917093, IEEE Journal of Biomedical and Health Informatics

(19)

And, the Kalman gain $\mathbf{K}_n$ could be shown as

$$\mathbf{K}_n = \left(\overline{\mathbf{P}}_{xy,n|n-1} \Big/ \mathbf{S}_{yy,n|n-1}^{\mathrm{T}}\right) \Big/ \mathbf{S}_{yy,n|n-1}, \quad (20)$$

where / denotes the right division operation on the matrix. Therefore, the estimation $\hat{\mathbf{x}}'_{n|n}$ of the states and the square-root $\mathbf{S}_{n|n}$ of the corresponding error-covariance matrix are obtained as

$$\hat{\mathbf{x}}'_{n|n} = \hat{\mathbf{x}}'_{n|n-1} + \mathbf{K}_n e_n, \quad (21)$$

$$\mathbf{S}_{n|n} = qr\left(\left[\mathbf{X}_{n|n-1} - \mathbf{K}_n \mathbf{Y}_{n|n-1}\right]\right), \quad (22)$$

where $\mathrm{e}_n = \mathrm{y}_n - \hat{\mathrm{y}}_{n|n-1}$. At this time, the estimation $\hat{\mathbf{x}}^a_{n|n}$ of the augmented state vector and its corresponding error-covariance matrix $\mathbf{S}^a_{n|n}$ can be given by

$$\hat{\mathbf{x}}^a_{n|n} = \left[\hat{\mathbf{x}}'_{n|n}, \mathbf{0}_{n_\mathbf{p}}, \mathbf{0}_{n_\mathbf{s}} \mathbf{0}_{n_\mathbf{v}}, \mathbf{0}_{n_\mathrm{m}}\right]^{\mathrm{T}}, \quad (23)$$

$$\mathbf{S}^a_{n|n} = diag\left(\mathbf{S}_{n|n}, \mathbf{S}_\mathbf{p}, \mathbf{S}_\mathbf{s}, \mathbf{S}_\mathbf{v}, \mathrm{S}_\mathrm{m}\right), \quad (24)$$

Finally, this algorithm will converge if

$$l_L \le \tilde{l}, \quad (25)$$

where $\tilde{l}$ is a threshold and l_n, $n = 1, 2, \ldots L$ is a likelihood function, which is given by

$$l_n = l_{n-1} - \left[\log(2\pi) L + \log\left|\mathbf{S}_{yy,n|n-1}\mathbf{S}^{\mathrm{T}}_{yy,n|n-1}\right| + \mathrm{e}_n^2 \Big/ \left(\mathbf{S}_{yy,n|n-1}\mathbf{S}^{\mathrm{T}}_{yy,n|n-1}\right)\right] \Big/ 2, \quad n = 1, 2, \ldots L \quad (26)$$

Table 1 gives the details of the forward filtering.

TABLE I
STEPS OF CSCKS ALGORITHM'S FORWARD FILTERING

Input:
BOLD signal y_n, $n = 1, 2, \ldots L$;
External input u_n.
Output:
Filtered estimation $\hat{\boldsymbol{x}}'_{n|n}$
Known condition:
State function $\mathbf{H}'_{n|n-1}(\cdot)$;
Observation function $\lambda_n(\cdot)$;
Filtered error-covariance matrices $\mathbf{Q}_{\mathbf{x},0|0}$, $\mathbf{Q}_{\boldsymbol{\theta},0|0}$, $\mathbf{Q}_{\boldsymbol{\beta},0|0}$ and their corresponding noise covariance matrices $\mathbf{Q}_\mathbf{p}$, $\mathbf{Q}_\mathbf{s}$, $\mathbf{Q}_\mathbf{v}$;
Noise covariance matrix Q_m of BOLD signal.
Steps:
I **Filter initialization**
①Initialize $\hat{\mathbf{x}}^a_{0|0}$ and $\mathbf{S}^a_{0|0}$ by (8) and (9), $n = 0$, $l_0 = 0$;
II **Time update step**
② $\hat{\mathbf{x}}'_{n|n-1}$ is obtained by (10-12);
③ $\mathbf{S}_{n|n-1}$ is obtained by (13-14);
III **Measurement update step**
④ $\hat{\mathbf{x}}'_{n|n}$ is obtained by (12) and (14-21);
⑤ $\mathbf{S}_{n|n}$ is obtained by (22);
⑥ $\hat{\mathbf{x}}^a_{n|n}$ and $\mathbf{S}^a_{n|n}$ are obtained by (23) and (24), respectively;
⑦ l_n is obtained by (16) and (26);
⑧ $n = n + 1$;
IV **Iterative judgment**
⑨If $n \le L$, repeat step II-III in Table 1. Otherwise, perform step I-III in Table 2.

C. Backward Smoothing

Forward filtering is used to achieve a preliminary estimation of the model parameters, and backward filtering is to smooth the results of the forward filtering to improve the estimation accuracy. Since the low frequency confounds are considered, the backward filtering of the algorithm also needs to rewrite the state vector, the filtered error-covariance matrix, the predicted error-covariance matrix and the cross-covariance matrix, as compared with the backward part of the original SCKS. Of course, these rewriting variables in the backward smoothing algorithm are combined with the forward filtering algorithm, where the backward smoothing has been described in detail in [3]. Therefore, this paper only gives the steps of the backward smoothing in Table 2. In addition, Tables 1 and 2 also give the condition for the end of iteration and loop for CSCKS algorithm.

TABLE II
STEPS OF CSCKS ALGORITHM'S FORWARD FILTERING

Input:
Filtered estimate $\hat{\mathbf{x}}'_{n|n}$, square-root factor $\mathbf{S}_{n|n}$, augmented filtered estimate $\hat{\mathbf{x}}^a_{n|n}$ and its augmented square-root factor $\mathbf{S}^a_{n|n}$, likelihood function l_n computed in Table 1, $n = 1, 2, \ldots L$.
Output:
Smoothed value $\hat{\mathbf{x}}^s_{n|n}$.
Known conditions:
State function $\mathbf{H}'_{n|n-1}(\cdot)$;
Filtered error-covariance matrix $\mathbf{Q}_{\mathbf{x},0|0}$, $\mathbf{Q}_{\boldsymbol{\theta},0|0}$, $\mathbf{Q}_{\boldsymbol{\beta},0|0}$ and its corresponding noise covariance matrix $\mathbf{Q}_\mathbf{p}$, $\mathbf{Q}_\mathbf{s}$, $\mathbf{Q}_\mathbf{v}$;
Noise covariance matrix Q_m of BOLD signal.
Steps:
I **Initialization:** $n = L$
II **Backward smoothing filtering step**

$$\boldsymbol{\chi}^a_{i,n-1|n-1} = \mathbf{S}^a_{n-1|n-1}\boldsymbol{\xi}_i + \hat{\mathbf{x}}^a_{n-1|n-1},$$
$$\boldsymbol{\chi}^{\mathbf{x},\boldsymbol{\theta},\boldsymbol{\beta}}_{i,n|n-1} = \mathbf{H}'\left(\boldsymbol{\chi}^{\mathbf{x}}_{i,n-1|n-1}, \boldsymbol{\chi}^{\boldsymbol{\theta}}_{i,n-1|n-1}, \boldsymbol{\chi}^{\boldsymbol{\beta}}_{i,n-1|n-1}\right) + \boldsymbol{\chi}^{\mathbf{p},\mathbf{s},\mathbf{v}}_{i,n-1|n-1},$$
$$\hat{\mathbf{x}}^s_{n|n-1} = \left(\sum_{i=1}^{\bar{m}} \boldsymbol{\chi}^{\mathbf{x},\boldsymbol{\theta},\boldsymbol{\beta}}_{i,n|n-1}\right) \Big/ \bar{m},$$
$$\mathbf{X}_{n|n-1} = \left[\boldsymbol{\chi}^{\mathbf{x},\boldsymbol{\theta},\boldsymbol{\beta}}_{1,n|n-1} - \hat{\mathbf{x}}^s_{n|n-1}, \boldsymbol{\chi}^{\mathbf{x},\boldsymbol{\theta},\boldsymbol{\beta}}_{2,n|n-1} - \hat{\mathbf{x}}^s_{n|n-1}, \ldots, \boldsymbol{\chi}^{\mathbf{x},\boldsymbol{\theta},\boldsymbol{\beta}}_{\bar{m},n|n-1} - \hat{\mathbf{x}}^s_{n|n-1}\right] \Big/ \sqrt{\bar{m}},$$
$$\mathbf{S}^s_{n|n-1} = qr\left(\left[\mathbf{X}_{n|n-1}\right]\right),$$
$$\mathbf{X}'_{n-1|n-1} = \left[\boldsymbol{\chi}^{\mathbf{x},\boldsymbol{\theta},\boldsymbol{\beta}}_{1,n-1|n-1} - \hat{\mathbf{x}}^{\mathbf{x},\boldsymbol{\theta},\boldsymbol{\beta}}_{n-1|n-1}, \boldsymbol{\chi}^{\mathbf{x},\boldsymbol{\theta},\boldsymbol{\beta}}_{2,n-1|n-1} - \hat{\mathbf{x}}^{\mathbf{x},\boldsymbol{\theta},\boldsymbol{\beta}}_{n-1|n-1}, \ldots, \boldsymbol{\chi}^{\mathbf{x},\boldsymbol{\theta},\boldsymbol{\beta}}_{\bar{m},n-1|n-1} - \hat{\mathbf{x}}^{\mathbf{x},\boldsymbol{\theta},\boldsymbol{\beta}}_{n-1|n-1}\right] \Big/ \sqrt{\bar{m}}$$
$$\mathbf{P}_{x'x,n|n-1} = \mathbf{X}'_{n-1|n-1}\mathbf{X}^{\mathrm{T}}_{n|n-1},$$
$$\mathbf{A}_n = \left(\mathbf{P}_{x'x,n|n-1} \Big/ \mathbf{S}^{s^{\mathrm{T}}}_{n|n-1}\right) \Big/ \mathbf{S}^s_{n|n-1},$$
$$\hat{\mathbf{x}}^s_{n-1|n-1} = \hat{\mathbf{x}}^{\mathbf{x},\boldsymbol{\theta},\boldsymbol{\beta}}_{n-1|n-1} + \mathbf{A}_n\left(\hat{\mathbf{x}}^s_{n|n} - \hat{\mathbf{x}}_{n|n-1}\right),$$
$$\mathbf{S}^s_{n-1|n-1} = qr\left(\left[\mathbf{X}'_{n-1|n-1} - \mathbf{A}_n\mathbf{X}_{n|n-1}, \mathbf{A}_n\mathbf{S}^s_{n|n}\right]\right),$$
$$n = n - 1$$

III **Iterative judgment**
If $n \ge 0$, repeat steps II-III in this table. Otherwise, perform step IV in this table.
IV **Loop judgment**
If (25) satisfies or the number of cycles exceeds a threshold, the algorithm ends. Otherwise, the current cycle estimate $\hat{\mathbf{x}}^a_{1|1}$ is taken as the initial value $\hat{\mathbf{x}}^a_{0|0}$, and steps II-IV of Table 1 and Step II-III of Table 2 are repeated.

VI. EXPERIMENT SETUP

A. Data Generation

The data of this experiment were generated according to the differential equation in (1). The specific hemodynamic model used is the Balloon-Windkessel model, its detailed equations, model parameters and corresponding parameters settings are shown in Table 3-4 and Table6. The external input of the data is the arrangement of the Gaussian functions of six different peaks in time. The peaks of these Gaussian functions are 1, 0.8, 1, 0.2, 0.9 and 0.4, respectively and the corresponding time points of the peaks are 10, 15, 27, 39, 47 and 55, respectively. In

TABLE III
STATE AND OBSERVATION EQUATIONS OF BALLOON-WINDKESSEL HEMODYNAMIC MODEL

$\dot{\mathbf{x}} = \mathbf{f}(\mathbf{x}, u, \boldsymbol{\theta})$	$y = g(\mathbf{x}, u, \boldsymbol{\theta})$
$\dot{x}_1 = \epsilon u - \kappa x_1 - \gamma(h_2 - 1)$	$y = V_0(k_1(1-h_4) + k_2(1-h_4/h_3)$
$\dot{x}_2 = x_1/h_2$	$+k_3(1-h_3)$
$\dot{x}_3 = (h_2 - h_3^{1/\alpha})/(\tau h_3)$	$k_1 = 4.3\rho N_u T_e$
$\dot{x}_4 = \left(h_2\left(1-(1-\rho)^{1/h_2}\right)\right)/\rho$	$k_2 = \rho R_s T_e \exp(E_s)$
$-h_3^{1/\alpha} h_4/h_3)/(\tau h_4)$	$k_3 = 1 - \exp(E_s)$
$\mathbf{x} = [\, x_1, h_2, h_3, h_4 \,]^{\mathrm{T}}$	
$\boldsymbol{\theta} = [\, \kappa, \gamma, \rho \,]^{\mathrm{T}}$	

Note: $h_i = \exp(x_i)$ makes h_i be constantly non-negative, $i = 2, 3$ and 4.

TABLE IV
PARAMETERS OF BALLOON-WINDKESSEL HEMODYNAMIC MODEL

	Description(Value)		Description(Value)
x_1	Vasodilatory signal	ρ	Resting oxygen extraction
h_2	Blood flow		fraction
h_3	Blood volume	y	BOLD signal
h_4	Deoxyhemoglobin content	V_0	Blood volume fraction(8)
ϵ	Neuronal efficiency	$k_{1\sim3}$	The constant coefficient
κ	Rate of signal decay	N_u	Frequency offset(40.3)
γ	Rate of flow dependent	T_e	Echo time(0.04)
	elimination	E_s	Region specific ratios
u	External input		of the echo(0.02)
τ	Hemodynamic transit time	R_s	Slope of intravascular
α	Grubb's exponent		Relaxation rate(25)

TABLE V
INTERPOLATION NUMBER AND CORRESPONDING INTEGRAL STEP LENGTH AND DATA LENGTH

$\tilde{I}$	2,3,4,5,6,7,8
Δt	0.5,0.33,0.25,0.2,0.17,0.14,0.13
L	120,180,240,300,360,420,480

TABLE VI
MODEL PARAMETERS SETTING IN DATA GENERATION

Model parameters	Value
$\mathbf{x}_0$	$[0,0,0,0]^{\mathrm{T}}$
$\boldsymbol{\theta}_0$	$[0.65,0.41,0.98,0.32,0.34,\ 0.02,0.5]^{\mathrm{T}}$
$\boldsymbol{\beta}$	$[2.4,-0.4,1.0,-0.8,0.6,0.2]^{\mathrm{T}}$
$\bar{L}$	6
Actual angular frequency $\bar{\omega}_n$	decreases from $0.55\,\pi$ to $0.67\,\pi$
Nominal angular frequency ω	$0.55\,\pi$
Correlation matrix $\mathbf{R}_c$	$\begin{bmatrix} 1 & 0.5 & 0.2 & 0 & 0 & 0 \\ 0.5 & 1 & 0.5 & 0.2 & 0 & 0 \\ 0.2 & 0.5 & 1 & 0.5 & 0.2 & 0 \\ 0 & 0.2 & 0.5 & 1 & 0.5 & 0.2 \\ 0 & 0 & 0.2 & 0.5 & 1 & 0.5 \\ 0 & 0 & 0 & 0.2 & 0.5 & 1 \end{bmatrix}$

particular, considering the influence of the integration step Δt of the data on the algorithm, cosine transform interpolation on data is required and the final Δt will be the interval between adjacent time points after interpolation. The time length of an original BOLD signal data is 60. The length L of interpolated data and the corresponding interpolation number $\tilde{I}$ and the integration step Δt are shown in Table 5. The data is specifically obtained from a Matlab file, spm_DEM_generate.m in the ToolBox directory of SPM12 software [3], and its download address is http://www.fil.ion.ucl.ac.uk/spm/. Finally, in order to evaluate

TABLE VII
STEPS OF CONFOUNDS GENERATION

Steps:

① Establish a matrix $\bar{\mathbf{W}} = \left[\bar{\boldsymbol{\Omega}}_1, \bar{\boldsymbol{\Omega}}_2, \ldots \bar{\boldsymbol{\Omega}}_{\bar{L}}\right]$,
Where $\bar{\boldsymbol{\Omega}}_n = \left[\sqrt{1/L}\cos 0\bar{\omega}_n n\Delta t, \sqrt{2/L}\cos 1\bar{\omega}_n n\Delta t\ , \ldots \sqrt{2/L}\cos\left(\bar{L}-1\right)\bar{\omega}_n n\Delta t\right]^{\mathrm{T}}$,
② Compute $\bar{\mathbf{W}}_c = \mathbf{R}_c^{1/2}\bar{\mathbf{W}}$,
③ Generate confounds $\bar{\mathbf{C}} = \boldsymbol{\beta}^{\mathrm{T}}\bar{\mathbf{W}}_c$.

the influence of confounds on algorithms, confounds need to be added to the data generated by the model, and is generated by equation (6). The maximum order of the harmonics and the actual angular frequency in the confounds are set from the heartbeat and breath frequency inducing the confounds [28], and the parameters and steps of generation are shown in Table 6-7.

B. Algorithm Setting

In order to evaluate the performance of CSCKS algorithm proposed in this paper, we compare it with the existing SCKS algorithm and DEM algorithm. In addition, the result of CSCKF is the forward filter value when the CSCKS algorithm converges, and the parameters and initialization conditions of the CSCKS and CSCKF algorithms are shown in Table 8. The detailed parameters of SCKS and DEM algorithms could be seen in [3], and the two algorithms here are realized from Matlab files, spm_SCK.m and spm_DEM.m in the ToolBox directory of SPM12.

TABLE VIII
PARAMETERS AND INITIAL CONDITION SETTING OF CSCKS ALGORITHM

$\hat{\mathbf{x}}_{0\mid 0} = [0,0,0,0]^{\mathrm{T}}$	$\mathbf{Q}_{\boldsymbol{\theta}.0\mid 0} = diag\left(10^{-20}, 10^{-20}, 10^{-20}\right)$
$\hat{\boldsymbol{\theta}}_{0\mid 0} = [\,\bar{\theta}_1, \bar{\theta}_2, \bar{\theta}_3\,]^{\mathrm{T}}$	$\mathbf{Q}_{\mathbf{n}} = diag\left(10^{-6}, 10^{-6}, 10^{-6}, 10^{-6}\right)$
$\bar{\theta}_i = \mathcal{N}\left(\theta_i^{true}, 1/10\right)$	$\mathbf{Q}_{\mathbf{s}} = diag\left(10^{-4}, 10^{-4}, 10^{-3}\right)$
$\boldsymbol{\theta}^{true} = [0.65, 0.41, 0.34]^{\mathrm{T}}$	$\mathbf{Q}_{\mathbf{v}} = diag\left(10^{-4}, 10^{-4}, 10^{-4}, 10^{-4}\right.$
$\hat{\boldsymbol{\beta}}_{0\mid 0} = [0,0,0,0,0,0]^{\mathrm{T}}$	$\left.10^{-4}, 10^{-4}\right)$
$\mathbf{Q}_{\mathbf{x}.0\mid 0} = diag\left(10^{-2}, 10^{-2}, 10^{-2}, 10^{-2}\right)$	$Q_m = diag\left(10^{-3}\right)$
$\mathbf{Q}_{\boldsymbol{\beta}.0\mid 0} = diag\left(10^{-3}, 10^{-3}, 10^{-3}, 10^{-3}\right.$	$l_0 = 0$
$\left.10^{-3}, 10^{-3}\right)$	$\tilde{I} = 10^{-3}$

In summary, we applied four schemes to the same simulated data under varying levels of confounds (i.e., SIR). The four schemes included DEM, SCK and two variance of the extended filtering scheme (CSCKS and CSCKF). These two variables refer to the results from smoothing and filtering respectively (i.e., forward and backward estimation and forward estimation only).

C. Experimental Methods

The Monte Carlo method was used for the experiments in this section, and all results were averaged from the results of 100 independent experiments. We conducted two groups of experiments under different integration steps and different SIR. The relevant parameters are as follows.

- Sampling interval (repetition time) TR = 1 second.
- Maximum number $\tilde{N}$ of loops in the algorithm is 32.
- The signal-to-noise ratio (SNR) is 20 dB, the SNR is defined as

$$SNR = 10\lg\left[\sum_{i=1}^{L}\left(y_i - \bar{y}\right)^2 \Big/ \sum_{j=1}^{L}\left(m_j\right)^2\right], \qquad (27)$$

This article has been accepted for publication in a future issue of this journal, but has not been fully edited. Content may change prior to final publication. Citation information: DOI 10.1109/JBHI.2019.2917093, IEEE Journal of Biomedical and Health Informatics

where $\bar{y}$ is the mean of $\mathbf{y}$, m is the measurement noise term in (7-b).

- The SIR is defined as

$$SIR = 10\lg\left[\sum_{i=1}^{L}(y_i-\bar{y})^2 \Big/ \sum_{j=1}^{L}\left(\boldsymbol{\beta}_j^{\mathrm{T}}\boldsymbol{\Omega}_j\right)^2\right], \qquad (28)$$

where $\bar{y}$ is the mean of $\mathbf{y}$.

- The amplitude a of the confounds and its corresponding SIR are shown in Table 9.

TABLE IX
CONFOUNDS' AMPLITUDE AND CORRESPONDING SIR

a	0.999,0.795,0.631,0.501,0.398,0.316,0.251,0.199,0.158,0.126
SIR	3,5,7,9,11,13,15,17,19,21

In the results of this experiment, we use the relative error to evaluate the performance of estimation, and define it as

$$\varepsilon = \left[\sum_{j=1}^{\tilde{n}}\sum_{i=1}^{\tilde{L}}\left|\hat{\mathbf{z}}_{ij}-\mathbf{z}_{ij}\right| \Big/ \sum_{j=1}^{\tilde{n}}\sum_{i=1}^{\tilde{L}}\left|\mathbf{z}_{ij}\right|\right]\times 100\%, \qquad (29)$$

where $\hat{\mathbf{z}}_{ij}$ and $\mathbf{z}_{ij}$ represent a estimated value and a true value in the i th iteration of the j th loop, respectively, $\tilde{n}$ denotes the number of the loops, $\tilde{n} \in [1, \tilde{N}]$, $\tilde{L}$ denotes the number of iterations.

VII. EXPERIMENTAL RESULTS AND ANALYSIS

A. Results under Fixed SIR and Integration Step

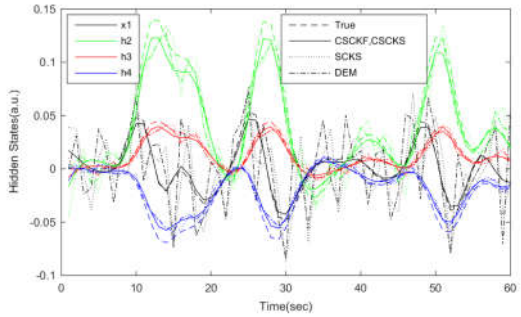

(a) Estimation results for the hidden states.

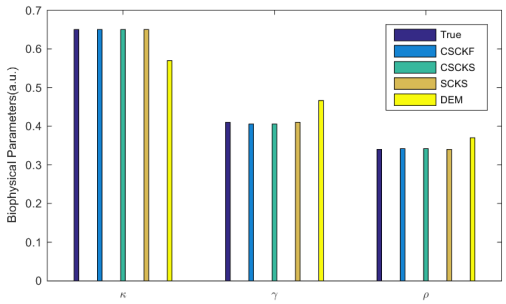

(b)Estimation results for biophysical parameters.

Fig. 2. Estimated result When SIR = 15 dB and Δt = 0.33 sec.

Firstly, the estimation curves of each algorithm under fixed SIR and integration step are given. Fig. 2 gives the estimation results of each algorithm when SIR = 15 dB and Δt = 0.33 seconds. The notation a.u. in y axis represents arbitrary unit [3]. In addition, as shown in Table 5, the length of the interpolated data corresponding to Δt = 0.33 is 180. Considering that the length of the original experimental data generated is 60, however, we only extract 60 time points, which are interpolated data at the 1st, 4th, and 7th … positions, intervals of 3. From the results of Fig. 2(a), the estimation curves of CSCKS and CSCKF algorithms for the hidden states are coincident, and the maximum deviation value is only about 0.02 compared with the real curve, and the estimated curve is smoother. The estimation curves of SCKS and DEM algorithms are also similar, but they deviate significantly from the real curves, for the green, red and blue estimation curves, the maximum deviation value reaches 0.04, for the black estimation curve, the maximum deviation value reaches about 0.07, and the estimation curve has large frequent fluctuations. The results show that the traditional SCKS and DEM have higher estimation error than CSCKS and CSCKF under such conditions of SIR and integration step. And, the performance of forward filtering and backward smoothing is the same in the proposed algorithm. In addition, we see that the estimation curves of CSCKS are delayed from the real curves, at about points 10, 25, 40 and 50. The reason is that the Kalman filter used by CSCKS needs to be iteratively updated through observations, and the tracking of the state is prone to lag. Fig. 2(b) shows the estimation curves for the biophysical parameters of the model. It can be seen from the figure that the deviation of the estimated values of κ from the real values by CSCKS, CSCKF and SCKS algorithms is less than 0.01, which achieves a better estimation. For γ and ρ, the estimation error of SCKS is also less than 0.01, and the estimation error of SCKS and CSCKF is about 0.02, which is slightly larger than SCKS algorithm. The maximum deviation of the parameter estimation by the DEM algorithm reaches 0.08, and the deviation is slightly larger than the previous three algorithms. Overall, the four algorithms have a good estimation of the model parameters.

To further evaluate the effect of SIR and integration step on the performance of the algorithms, we will give experimental results from the following two aspects.

B. Results under Variant SIR

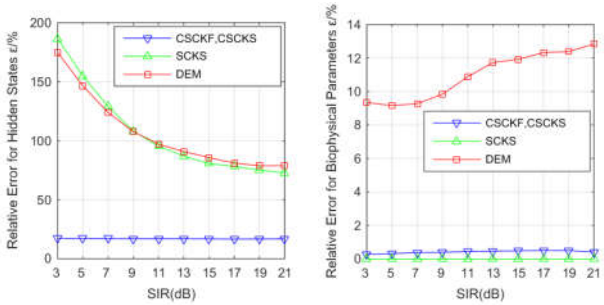

(a) Error curves for hidden states (b) Error curves for biophysical parameters.

Fig. 3. Estimation error curves at different SIR when Δt = 0.33 sec.

The experiments in this subsection consider the effect of SIR on the estimation of the algorithm. Fig. 3 shows the relative error curve of each algorithm changing with SIR when Δt = 0.33 seconds. From Fig. 3(a), we can see that as the SIR increases from 3 dB to 21 dB, the relative errors of CSCKS, CSCKF, SCKS, and DEM algorithms for the hidden states are reduced from 17%, 17%, 187%, and 175% to 16%, 16%, 73%, and 79%, respectively. Besides, regardless of how SIR changes, the CSCKS curve is always below the SCKS and DEM curves

This article has been accepted for publication in a future issue of this journal, but has not been fully edited. Content may change prior to final publication. Citation information: DOI 10.1109/JBHI.2019.2917093, IEEE Journal of Biomedical and Health Informatics

in Fig. 3(a), ie, the estimated error is smaller than the SCKS and DEM algorithms. In addition, it is also noted that the relative errors curves of SCKS and DEM have an intersection at about $SIR = 9$ dB. When SIR is less than 9 dB, the relative error of the latter is smaller than the former, and when it is greater than 9 dB, the situation is the opposite. This shows that under the small SIR, the relative error of the DEM is smaller than the SCKS algorithm. Fig. 3(b) shows the relative error estimation curves of the four algorithms for biophysical parameters. For CSCKF/CSCKS and SCKS, the three curves are CSCKF/CSCKS and SCKS from high to low, and the relative error values vary from 0.2% to 0.5% and around 0.01% respectively, and their minimum errors and maximum errors do not differ by more than 1%. The results show that the change of SIR has little effect on the parameters estimation of the CSCKF/CSCKS and SCKS algorithms, and the estimation errors of the three algorithms are maintained at a low level. The relative error range of DEM is 9%-13%, and the estimation error is significantly higher than the CSCKF/CSCKS and SCKS algorithms and it is hardly affected by the SIR.

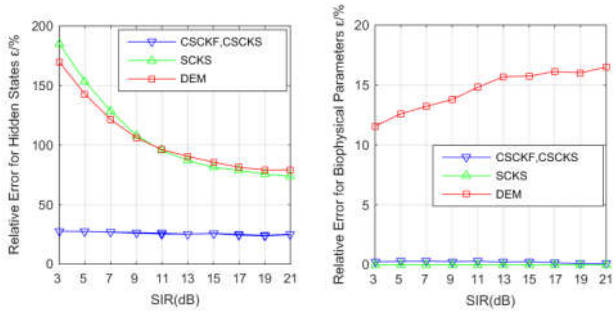

(a) Error curves for hidden states (b) Error curves for biophysical parameters.

Fig. 4. Estimation error curves at different SIR when $\Delta t = 0.13$ sec.

Fig. 4 shows the estimated curves when $\Delta t = 0.13$ seconds. Similar with Fig. 3(a), the estimation error curves for the hidden states in Fig. 4(a) also decrease as SIR increases. In addition, regardless of how SIR changes, the CSCKS curve is always below the SCKS and DEM curves in Fig. 3(a), which still shows that the estimated error of CSCKS is smaller than SCKS and DEM. In addition, the intersection of SCKS and DEM curves in Fig. 4(a) is about SIR is 11 dB. This result means that the estimated error of DEM is smaller than SCKS under smaller SIR. The high to the low order of the curves in Fig. 4(b) is also the same as the curves of Fig. 3(b), and the error range is between 0%-17%, which is also similar to Fig. 3(b). In addition, it should be noted that the curves of CSCKF and CSCKS are not completely coincident compared with the previous results, which indicates that the smoothing part would affect the algorithm.

C. Changing the Integration Step

In this subsection, the experiments consider the influence of the integral step on the estimation results of the algorithms. Fig. 5 shows the relative error curves of the four algorithms changing with integration step under a small signal-to-interference ratio $SIR = 3$ dB. It can be seen from Fig. 5(a) that the relative errors of SCKS and DEM both reach 170%, and the curves do not change much with the integration step.

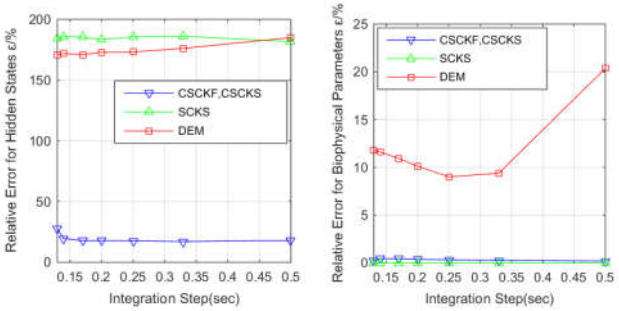

(a) Error curves for hidden states (b) Error curves for biophysical parameters.

Fig. 5. Estimation error curves at different Δt when $SIR = 3$ dB.

On the other hand, the two curves of CSCKS and CSCKF coincide, and are around 20%, except 28% at the integration step size of about 0.13 seconds. This result shows that under lower SIR, the integration step does not improve the estimation performance of the traditional SCKS and DEM algorithms, and the small integration step increases the estimation error of CSCKS. Fig. 5(b) shows the relative error of the biophysical parameters estimated by the four algorithms changing with integration step at $SIR = 3$ dB. The error curve of CSCKS algorithm increases first and then decreases as the integration tep increases, reaching a peak of 0.4% at about 0.14 second, and tending to be 0.2% at other times. Overall, the estimation errors of the CSCKF/CSCKS and SCKS algorithms are all less than 0.5%, which indicates that the three algorithms have a good estimation of biophysical parameters. In addition, contrary to the error estimation curve of CSCKS, the DEM algorithm decreases first and then increases with the integration step, and its minimum trough value exceeds 9%. Compared with the other three algorithms, it has a large estimation error. It is worth noting that the results of SCKS in Fig. 5 is the same as those in Fig. 3 and 4, and the error is still maintained at 0.01%. The reason is that the error covariance of the biophysical parameter in the original implementation spm_SCK.m of the algorithm is set to a small value.

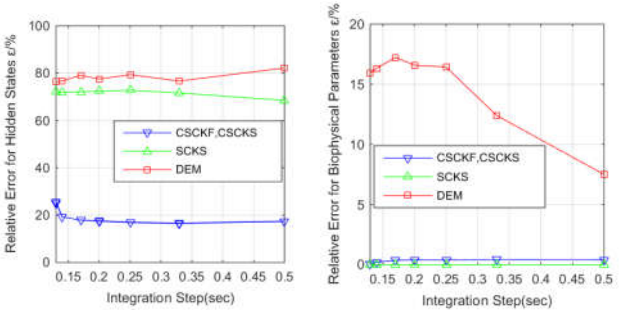

(a) Error curves for hidden states (b) Error curves for biophysical parameters.

Fig. 6. Estimation error curves at different Δt when $SIR = 21$ dB

Fig. 6(a) shows the relative error curves of the hidden states estimated by the four algorithms changing with integration step at higher $SIR = 21$ dB. As can be seen from Fig. 6(a), the four curves are arranged from high to low as DEM, SCKS and CSCKF/CSCKS, where the minimum relative error of DEM is approximately 76%, and is less affected by the variation of the integration step. The estimation error of SCKS also decreased from about 72% to 68% with the increase of the integration step, which only changed by 4%. On the other hand, the trend of the

This article has been accepted for publication in a future issue of this journal, but has not been fully edited. Content may change prior to final publication. Citation information: DOI 10.1109/JBHI.2019.2917093, IEEE Journal of Biomedical and Health Informatics

curves of CSCKS and CSCKF is the same as that of Fig. 5 and their relative errors are around 18% except a larger value 26% at the integration step $\Delta t = 0.13$ seconds. This result shows that under higher SIR, the integration step has little effect on the estimation performance of the four algorithms. Fig. 6(b) shows the relative error of the biophysical parameters estimated by the four algorithms changing with integration step at $SIR = 21$ dB. The implementation trend of the four algorithms in the figure is also consistent with the results of Fig. 5. The estimation error of the CSCKF/CSCKS and SCKS algorithms all does not exceed 1%, which indicates that under higher SIR, the three algorithms have a good estimation for the biophysical parameters regardless of the integration step. However, the relative error curves of the DEM algorithm increases first and then decreases with the integration step, and its maximum peak value reaches 17%, indicating that the estimation of biophysical parameters is slightly worse than the other three algorithms.

VIII. Discussion

In this paper, we study how to estimate the hidden states and biophysical parameters from fMRI observation signals. In experiments, we compare the proposed CSCKS algorithm with existing SCKS and DEM schemes. However, there are some problems which need further discussion about the model and the estimation algorithms.

The first problem is to compare the proposed Kalman filter with a linear regression method, especially in environment with real fMRI data. Since confounds are expressed as some trigonometric functions with fixed angular frequencies, can a linear regression estimate and remove the confounds? For this, we download a group of real fMRI data, MoAEpilot.zip from SPM (Statistical Parametric Mapping) website https://www.fil.ion.ucl.ac.uk/spm/data/Auditory. This data is preprocessed by SPM12 software, including realignment, coregistration, normalization, smooth and adjustment. The coordinates of the extracted BOLD signal are (60, -19, 11). With the real data, we then compare the performance of a linear regression with our CSCKS. Note that the hemodynamic model in this paper is a differential non-linear model and a linear regression is not easy to directly apply to it. Thus, we consider a linear convolutional model [33] shown in Fig. 7(a). Through the real BOLD signal, the linear regression can estimate a scale coefficient called β [33]. After a statistical test on β, it can be inferred whether the location of the BOLD signal is active. Fig. 7(c) gives the estimation of the linear regression and CSCKS. From the figure, the value of β estimated by SCKS without considering the confounds deviates much from the expected values than the other two algorithms. On the other hand, the β curve estimated by CSCKS fluctuates around the expected β while the method of linear regression differs from the expected β by one. One likely reason is that in addition to the presence of confounds, there may be other noises, such as Gaussian noise. Therefore, CSCKS has better estimation performance than Linear. In addition, as can be seen from the figure, the β curve of CSCKS has a higher resolution. Since CSCKS is a successive state estimation, it can exhibit the change of β with time. In contrast, the linear method treats β as a constant, so it does not change over time.

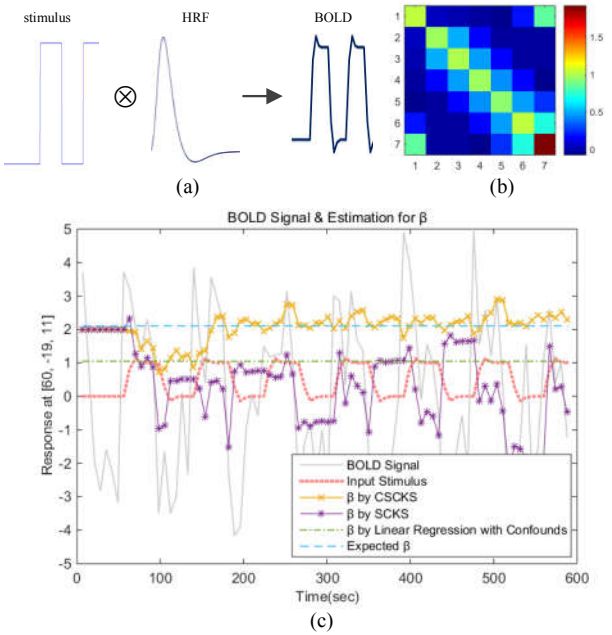

Fig. 7. (a) A convolutional model for BOLD signal, (b) A correlation matrix for confounds with input signal, (c) Estimation of β in a real fMRI data.

Second, the confounds in fMRI data should be correlated with input stimuli. If the additive confounds is modeled as a completely independent fluctuation from the input stimuli, this may not be the case sometimes. In reality, both cardiac and respiration can be correlated with the task timing. The correlation with the input stimuli is the reason why these confounds become so hard to deal with. In fact, we analyzed the frequency of the input stimuli in the simulation experiment above and then make the frequency of the confounds and that of the input have overlaps. Fig. 7(b) gives the computational results of the correlation matrix of confounds with the input stimuli. From the figure, the correlation value of the input stimuli with 6th component in the confounds is about 0.8, which displays some correlation between them.

Finally, dose the estimation of the extra parameter, i.e. the coefficients of the confounds increases the chance of falling into false positive? For the traditional SCKS, it not only estimates the hidden state and biophysical parameters, but also estimates the input stimulus. However, in some fMRI experiments for brain cognitive, these external stimuli can be pre-designed and thus be treated as a known variable. Therefore, sometimes the estimation of the input is not needed. Although the coefficient vector of the confounds is introduced to CSCKS, the coefficient of the confounds replace the input. That is, the original estimate has three items and it still has three items now. This will not cause the equation to become an indefinite equation.

IX. Conclusion

The problem studied in this paper is to estimate the hidden states and biophysical parameters in a hemodynamic model by

fMRI observation signals. Since the fMRI signal is susceptible to confounds signals, we consider a state space equation for a hemodynamic model with confounds. For this augmented state space model, we propose a CSCKS algorithm to improve estimated performance under confounds. In experiments, we use a Balloon-Windkessel model to generate simulation data. The estimation error of the proposed CSCKS algorithm was compared with existing SCKS and DEM schemes under different SIR and integration step, we obtained the following important results.

When the integration step is fixed and SIR is less than 21 dB, the relative error of the existing SCKS and DEM algorithms for the estimation of hidden states is more than 73%, and the relative minimum error of the proposed CSCKS algorithm is only 16%. In addition, when SIR is fixed and the integration step is less than 0.14 seconds, the maximum relative error of CSCKS is 28%, and when it is greater than 0.14 seconds, the error can be reduced to 20%. In summary, when SIR is lower, the proposed CSCKS algorithm for the hidden state estimation has less error than the existing algorithms, and too small integration step will increase the estimation error of the proposed algorithm.

The code for the CSCKS and CSCKF algorithms proposed in this article has been uploaded to GitHub, and its download address is https://github.com/lumingzhi/CSCKF-CSCKS.

ACKNOWLEDGMENT

We would like to thank K.J. Friston for his valuable advice and modifying a lot of sentences in detail, The Wellcome Department of Imaging Neuroscience, University College London. We would also like to thank our reviewers for their upcoming academic guidance.

REFERENCES

[1] O. David, "fMRI connectivity, meaning and empiricism Comments on: Roebroeck et al. The identification of interacting networks in the brain using fMRI: Model selection, causality and deconvolution," NeuroImage, vol. 58, no. 2, pp. 306-309, Sep. 2009.

[2] K.J. Friston, "Dynamic casual modeling and Granger causality Comments on: The identification of interacting networks in the brain using fMRI: Model selection, causality and deconvolution," NeuroImage, vol. 58, no. 2, pp. 303-305, Sep. 2009.

[3] M. Havlicek, K.J. Friston, J. Jan, M. Brazdil, and V.D. Calhoun, "Dynamic modeling of neuronal responses in fMRI using cubature Kalman filtering," NeuroImage, vol. 56, no. 4, pp. 2109-2128, 2011.

[4] H.I. Suk, C.Y. Wee, S.W. Lee, and D. Shen, "State-space model with deep learning for functional dynamics estimation in resting-state fMRI," NeuroImage, vol. 129, pp. 292-307, Sep. 2016.

[5] A.X. Patel, and E.T. Bullmore, "A wavelet-based estimator of the degrees of freedom in denoised fMRItime series for probabilistic testing of functional connectivity andbrain graphs," NeuroImage, vol. 142, pp. 14-26, Nov. 2016.

[6] R.M. Birn, Z.S. Saad, and P.A. Bandettini, "Spatial heterogeneity of the nonlinear dynamics in the FMRI BOLD response," NeuroImage, vol. 14, no. 4, pp. 817-826, Nov. 2001.

[7] A. Mechelli, C.J. Price, and K.J. Friston, "Nonlinear coupling between evoked rCBF and BOLD signals: a simulation study of hemodynamic responses," NeuroImage, vol. 14, no. 4, pp. 862-872, Nov. 2001.

[8] K.J. Friston, A. Mechelli, R. Turner, and C.J. Price, "Nonlinear responses in fMRI: the Balloon model, Volterra kernels, and other hemodynamics," NeuroImage, vol. 12, no. 4, pp. 466-477, 2000.

[9] K.A. Kurkela, and N.A. Dennis, "Event-related fMRI studies of false memory: An Activation Likelihood Estimation meta-analysis," NeuroImage, vol. 81, no. 6, pp. 149-167, Dec. 2016.

[10] K.J. Friston, "Bayesian estimation of dynamical systems: an application to fMRI," NeuroImage, vol. 16, no. 2, pp. 513-530, Jul. 2002.

[11] K.J. Friston, "Dynamic causal modelling," NeuroImage, vol. 19, no. 4, pp. 1273-1302, Aug. 2003.

[12] C.M. Ting, A.K. Seghouane, S.H. Salleh, and A.M. Noor, "Estimating Effective Connectivity from fMRI Data Using Factor-based Subspace Autoregressive Models," IEEE Signal Processing Letters, vol. 22, no. 6, pp. 757-761, Oct. 2015.

[13] D. Degras, and M.A. Lindquist, "A hierarchical model for simultaneous detection and estimation in multi-subject fMRI studies," NeuroImage, vol. 98, no. 7, pp. 61-72, 2014.

[14] B. Biswal, F.Z. Yetkin, V.M. Haughton, and J.S. Hyde, "Functional connectivity in the motor cortex of resting human brain using echo-planar MRI," NeuroImage, vol. 34, no. 4, pp. 537-541, Oct. 1995.

[15] G. Krüger, G.H. Glover, "Physiological noise in oxygenation sensitive magnetic resonance imaging," Magnetic Resonance in Medicine, vol. 46, no. 4, pp. 631-637, 2001.

[16] J.J. Riera, J. Watanabe, I. Kazuki, M. Naoki, E. Aubert, T. Ozaki, and R. Kawashimaa, "A state-space model of the hemodynamic approach: nonlinear filtering of BOLD signals," NeuroImage, vol. 21, no. 2, pp. 547-567, Mar. 2004.

[17] W. Liu, S.P. Awate, J.S. Anderson, P.T. Fletcher, "A functional network estimation method of resting-state fMRI using a hierarchical Markov random field," NeuroImage, vol. 100, pp. 520-534, Jun. 2014.

[18] J.C. Jimenez, and T. Ozaki, "Local linearization filters for non-linear continuous-discrete state space models with multiplicative noise," International Journal of Control, vol. 76, no. 12, pp. 1159-1170, Aug. 2003.

[19] L.A. Johnston, E. Duff, I. Mareels, and G.F. Egan, "Nonlinear estimation of the BOLD signal," NeuroImage, vol. 40, no. 2, pp. 504-514, Apr. 2008.

[20] L. Murray, A.J. Storkey, "Continuous time particle filtering for fMRI," in Proceedings of the Twenty-First Annual Conference on Neural Information Processing Systems, Vancouver, Canada, 2007, pp. 1049-1056.

[21] Z. Fu, S.C. Chan, X. Di, B. Biswal, and Z. Zhang, "Adaptive Covariance Estimation of Non-Stationary Processes and its Application to Infer Dynamic Connectivity From fMRI," IEEE Trans. Biomed. Circ. Syst, vol. 8, no. 2, pp. 228-239, Apr. 2014.

[22] Z. Hu, X. Zhao, H. Liu, and P. Shi, "Nonlinear analysis of the BOLD signal," EURASIP Journal on Advances in Signal Processing, vol. 2009, no. 1, pp. 1-13, Jan. 2009.

[23] K.J. Friston, N. Trujillo-Barreto, and J. Daunizeau, "DEM: a variational treatment of dynamic systems," NeuroImage, vol. 41, no. 3, pp. 849-885, Aug. 2008.

[24] R.B. Buxton, E.C. Wong, and L.R. Frank, "Dynamics of blood flow and oxygenation changes during brain activation: the balloon model," Magnetic Resonance in Medicine, vol. 39, no. 6, pp. 855-864, 1998.

[25] J.B. Mandeville, J.J. Marota, C. Ayata, G. Zaharchuk, M.A. Moskowitz, B.R. Rosen, and R.M. Weisskoff, "Evidence of a cerebrovascular postarteriole windkessel with delayed compliance," Journal of Cerebral Blood Flow and Metabolism, vol. 19, no. 6, pp. 679-689, Jun. 1999.

[26] W.Y. Ahn, A. Krawitz, W. Kim, J.R. Busmeyer, and J.W. Brown, "A Model-Based fMRI Analysis with Hierarchical Bayesian Parameter Estimation," Journal of Neuroscience Psychology and Economics, vol. 4, no. 2, pp. 95-110, May. 2011.

[27] S. Grootoonk, C. Hutton, J. Ashburner, A.M. Howseman, O. Josephs, G. Rees, K.J. Friston, and R. Turner, "Characterization and Correction of Interpolation Effects in the Realignment of fMRI Time Series," NeuroImage, vol. 11, no. 1, pp. 49-57, Feb. 2000.

[28] K. Murphy, R.M. Birn, and P.A. Bandettini, "Resting-state FMRI confounds and cleanup," NeuroImage, vol. 80, no. 1, pp. 349-359, Oct. 2013.

[29] S.A. Rombouts, C.J. Stam, J.P. Kuijer, P. Scheltens, and F. Barkhof, "Identifying confounds to increase specificity during a "no task condition". Evidence for hippocampal connectivity using fMRI," NeuroImage, vol. 20, no. 2, pp. 1236-1245, Oct. 2003.

[30] A.P. Holmes, O. Josephs, C. Buchel, and K.J. Friston, "Statistical modeling of low-frequency confounds in fMRI," NeuroImage, vol. 5, no. 4, pp. S480, Jan. 1997.

[31] M.Z. Lu, H.F. Wu, and Y. Zeng, "A New Algorithm for Solving Hemodynamic Models in fMRI under Low Frequency Interference," in Procedia Computer Science, Xiamen, China, vol. 131, 2018, pp. 485-494.

[32] S.P. Zhang, Y.P. Zhao, G.F. Shen, and S.Q. Zhang, "The Study of Removing Low-frequency Interference from Signal by IIR Lattice Notch Filter," Chinese Journal of Scientific Instrument, vol. 24, no. 4, pp. 508-511, 2003.
[33] K. J. Friston, J. T. Ashburner, S. J. Kiebel, T. E. Nichols and W. D. Penny, Statistical Parametric Mapping: The Analysis of Functional Brain Images. London, U.K.: Academic Press, pp. 101-210, 1995.

Haifeng Wu received the MS degree in electrical engineering from Yunnan University, Kunming, China, in 2004, and the PhD degree in electrical engineering from Sun Yat-Sen University, Guangzhou, China, in 2007. He was selected an associate professor of Yunnan Minzu University in 2010, and has been a professor since 2012. Prior to that, he was a postdoctoral scholar in the Kunchuan Institute of Technology from 2007 to 2009. In 2014, Prof. Wu was selected as the 17th Batch of Young and Middle-aged Leaders in Academic and Technical Reserved Talents of Yunnan Province, and was awarded three prizes for natural science of Yunnan Province in 2015. From 2015 to 2018, Prof. Wu was hired as a Distinguished Professor of Yunnan Minzu University. His research interests include signal processing, machine learning. Now, he has published multiple papers on peer-reviewed journals, such as IEEE Transactions, IEEE Journal and IEEE Letters.

Mingzhi Lu received the BS degree from Zhongyuan University of Technology, China, in 2015. He is working toward the graduate degree in the School of Electrical and Information Technology, Yunnan Minzu University, China. His research interests include machine learning and signal processing for fMRI.

Yu Zeng received MSc degrees from Yunnan University, China, in 2006.She is now working as a Lecturer in the School of Electrical and Information Technology, Yunnan Minzu University, China. Her research interests include signal processing, and machine learning.